Vacancies in SnSe single crystals in a near-equilibrium state

K. Sraitrova,[1] J. Cizek,[2] V. Holy,[3,4] T. Plechacek,[1] L. Benes,[1] M. Jarosova,[5] V. Kucek,[1] and C. Drasar[1,*]

[1]*University of Pardubice, Faculty of Chemical Technology, Studentska 573, 53210 Pardubice, Czech Republic*
[2]*Department of Low Temperature Physics, Faculty of Mathematics and Physics, Charles University, V Holesovickach 2, 18000 Praha 8, Czech Republic*
[3]*Department of Condensed Matter Physics, Faculty of Mathematics and Physics, Charles University, Ke Karlovu 3, 121 16 Praha 2, Czech Republic*
[4]*Masaryk University, Department of Condensed Matter Physics and CEITEC, Kotlarska 2, 61137 Brno, Czech Republic*
[5]*Institute of Physics of the CAS, v.v.i., Cukrovarnicka 10, 162 00 Prague 6, Czech Republic*

The development of intrinsic vacancies in SnSe single crystals was investigated as a function of annealing temperature by means of positron annihilation spectroscopy accompanied by transport measurements. It has been demonstrated that two types of vacancies are present in single-crystalline SnSe. While Sn vacancies dominate in the low-temperature region, Se vacancies and vacancy clusters govern the high-temperature region. These findings are supported by theoretical calculations enabling direct detection and quantification of the most favorable type of vacancies. The experiments show that Sn vacancies couple with one or more Se vacancies with increasing temperature to form vacancy clusters. Interestingly, the clusters survive the $\alpha \rightarrow \beta$ transition at $\approx$800 K and even grow in size with temperature. The concentration of both Se vacancies and vacancy clusters increases with temperature, similar to thermoelectric performance. This indicates that the extraordinary thermoelectric properties of SnSe are related to point defects. We suggest that either these defects vary the band structure in favor of high thermoelectric performance or introduce an energy-dependent scattering of free carriers realizing, in fact, energy filtering of the free carriers. Cluster defects account for the glasslike thermal conductivity of SnSe at elevated temperatures.

I. INTRODUCTION

The utilization of thermoelectric generators is an alternative for the recovery of waste heat. Research on thermoelectric (TE) materials is thus a very active field of research. The TE efficiency of a material can be expressed in terms of the dimensionless figure of merit, ZT, where $ZT = S^2 \sigma T / \kappa$. In this formula, S, σ, T, and κ are the Seebeck coefficient, electrical conductivity, absolute temperature, and thermal conductivity of the material, respectively [1]. Recently, high-TE performance has been reported for doped and undoped single-crystal SnSe or its solid solutions with SnS [2–4]. However, undoped polycrystalline SnSe shows only moderate TE performance according to Ref. [5]. The reason is still a point to debate, and doping seems to provide only minor improvements in polycrystals. As SnSe crystallizes in a complex structure below 810 K [6] with an inherently low thermal conductivity, there seems to be enough space for the tuning of other TE coefficients independently. However, a reinvestigation of its thermal conductivity has shown that the intrinsic thermal conductivity of a SnSe single crystal might be much higher than reported previously [7]. Furthermore, long-term stability seems to be questionable for doped samples [8]. Thus, an efficient and stable dopant of polycrystalline material is needed to increase the electrical conductivity to its TE optimum [9]. An

increasing number of doping studies have appeared each year since the first report [8,10–14]. With the aim of understanding the exceptional properties of SnSe, a number of studies of the band structure of SnSe have appeared [15–17]. The studies suggest that the TE performance of *n*-type materials is higher than that of *p*-type materials. This is corroborated by the latest results on Bi-doped *n*-type single crystals [18]. In Ref. [19], an unprecedented ZT value of 2.8 was reported for out-of-plane transport in *n*-type crystals. According to Ref. [20], quasi-two-dimensional (2D) transport is responsible for the excellent TE properties of SnSe.

Recently, more particular attention has been given to intrinsic defects (IDs) [15,21–23]. The intrinsic defects, e.g., Sn vacancies (V_{Sn}), seem to play a very important role in the excellent electronic properties of SnSe at elevated temperatures [15,24]. In Ref. [15], the authors suggest that the concentration of V_{Sn} increases rapidly with temperature with a formation energy of 0.67 eV and mimics thermal activation (excitation) of the free charge carriers from these defects. The excitation energy of the defects is much smaller [21]. Such activation leads to a large concentration of free carriers (FCs), thus increasing electrical conductivity. The corresponding decrease in the Seebeck coefficient is moderate due to the peculiar structure (and corresponding electronic structure) variations with increasing temperature [19]. In fact, a high concentration of V_{Sn} (5%) would modify the band structure towards higher FC effective masses and thus lead to a higher Seebeck coefficient [21]. We are left with the

question of how to preserve such a high concentration of V_{Sn} in a required temperature range. Equilibrium drives a tin under stoichiometric composition towards the formation of the secondary phase $SnSe_2$ instead of the formation of V_{Sn} at all temperatures [25].

Together with V_{Sn}, another intrinsic defect, interstitial Se (Se_i), seems to play an important role in transport properties; an extra-large concentration of this defect might be responsible for extremely low thermal conductivity [22]. Such intrinsic defects would provide excellent TE performance even at lower temperatures if induced artificially. However, it is not clear how to induce these defects in the required (lower) temperature range or stabilize them upon cycling. Again, excess Se should react to produce $SnSe_2$ [25].

The equilibrium concentration of IDs is generally a function of temperature. Data about the thermal stability and equilibrium stoichiometry as a function of temperature are missing in the literature from both experimental and theoretical perspectives. In the present paper, we observe that SnSe varies slightly with temperature; the structure of SnSe itself prefers a tin-poor state in the low-temperature range and a selenium-poor state at elevated temperatures. This fact alone implies that the physical properties will be a function of the starting stoichiometry but also of the kinetics of growth.

According to our experiments, it is highly plausible that the wide spectrum of outputs reported for SnSe single crystals (SCs) and polycrystals (PCs) in the literature is affected by the thermal history of the respective samples. In other words, the kinetics rather than the thermodynamics of sample preparation and, in most cases, the kinetics of measurements markedly affect the outputs. To shed more light on this issue, in the present work, stoichiometric single crystal (SC) samples were prepared and annealed for a prolonged time at various temperatures to achieve an equilibrium-close state for the respective temperatures. After annealing, the samples were quenched in air to preserve this state. Accordingly, all characterizations were performed below 450 K to prevent any aging of the samples. P-type conduction is ascribed to Sn vacancies in the literature [15,24]. In the present paper, it is demonstrated that this applies to the low-temperature region only. Using positron annihilation spectroscopy (PAS) accompanied by transport measurements, the nature of the intrinsic defects was characterized as a function of temperature. These investigations provided clear evidence that Se vacancies and the complex of vacancies dictate the p-type conductivity of SnSe above 500 K.

II. EXPERIMENTAL

A. Crystal growth

Stoichiometric single crystals of SnSe were grown by heating a mixture of 5N Sn and Se (both from Sigma-Aldrich). A stoichiometric mixture of elements was loaded into quartz ampoules and sealed under vacuum ($p < 10^{-3}$Pa). Then, the ampoules were heated to 1223 K at a rate of 1.7 K/min and kept at this temperature for 6 h. Crystal growth involved cooling at a rate of 0.1 K/min to 1073 K. The crystals were annealed at this temperature for 168 h. Subsequently, one of the ampoules was quenched in air, and the rest of them were

further cooled (0.1 K/min) to 973 K. The ampoules were kept at this temperature for 168 h, and one of them was quenched in air. This process was repeated using lower and lower temperatures until a temperature of 473 K was reached. Thus, a series of samples quenched from annealing temperatures (ATs) of 1073, 973, 873, 793, 773, 673, 623, 603, 573, and 473 K was prepared. These temperatures are used as labels for each sample (e.g., 473 K AT). Another series of stoichiometric SCs was prepared for comparison. In this case, the ampoules were slowly heated (1.7 K/min) up to 1223 K and then annealed at this temperature for 6 h. Subsequently, the ampoules were slowly cooled (0.1 K/min) to room temperature (293 K). It is assumed that this procedure is fast enough to prevent the SCs from reaching an equilibrium-close state at any temperature but room temperature. The sample prepared in such a way was used as a standard (denoted 293 K AT).

B. Positron annihilation

A carrier-free ^{22}Na radioisotope with an activity of ≈ 1 MBq deposited on a 2-μm-thick Mylar foil was used as a positron source for PAS. Two complementary PAS techniques were employed: positron lifetime (LT) spectroscopy [26], which enables the identification of defects and the determination of their concentrations, and coincidence Doppler broadening (CDB) [27], which provides information about the local chemical environment of the defects. PAS measurements were carried out at room temperature.

A digital spectrometer described in Ref. [28] was employed for the LT measurements. The spectrometer has a time resolution of 145 ps (full width at half maximum of the resolution function). The LT spectra, which always contained at least 10^7 positron annihilation events, were decomposed using a maximum-likelihood code [29]. The source contribution to the LT spectra consisted of two components with lifetimes of ≈ 368 ps and ≈ 1.5 ns and relative intensities of ≈ 11 and $\approx 1\%$, representing the contributions of positrons annihilating inside the ^{22}Na source spot and in the covering Mylar foil, respectively.

The CDB studies were carried out using a digital spectrometer [30] equipped with two high-purity Ge detectors and characterized by an energy resolution of 0.9 keV at the annihilation line of 511 keV and a peak-to-background ratio higher than 10^5. At least 10^8 annihilations were collected in each two-dimensional CDB spectrum. Subsequently, the CDB spectra were reduced into one-dimensional cuts representing the resolution function of the spectrometer and the Doppler-broadened annihilation peak. The results of the CDB measurements are presented as ratio curves with respect to Al; i.e., normalized Doppler-broadened peaks were divided by the normalized peak for a well-annealed pure Al (99.9999%) reference sample to highlight changes in the momentum distribution in the high-momentum region.

C. *Ab initio* calculations

Positron annihilation-related parameters (positron lifetimes and the momentum distribution of annihilating electron-positron pairs) were obtained by density-functional theory (DFT) *ab initio* calculations within the so-called standard

scheme [31]. In this approximation, the positron density is assumed to be vanishingly small everywhere and to not affect the bulk electron structure. First, the electron density $n(r)$ in the material is solved without the positron. Subsequently, the effective potential for the positron is constructed as

$$V_+(\boldsymbol{r}) = \phi(\boldsymbol{r}) + V_{\text{corr}}[n, \boldsymbol{\nabla} n], \quad (1)$$

where $\phi(\boldsymbol{r})$ is the Coulomb potential produced by the charge distribution of the electrons and nuclei, and V_{corr} is the zero-positron density limit of the electron-positron correlation potential [31].

The ground-state positron wave function was calculated by a numerical solution of the single-particle Schrödinger equation

$$-\frac{1}{2}\boldsymbol{\nabla}^2\psi_+(\boldsymbol{r}) + V_+(\boldsymbol{r})\psi_+(\boldsymbol{r}) = E_+\psi_+(\boldsymbol{r}), \quad (2)$$

where E_+ is the positron ground-state energy.

The positron lifetime was calculated from the overlap of the positron density $n_+(\boldsymbol{r}) = |\psi_+(\boldsymbol{r})|^2$ and the electron density $n(\boldsymbol{r})$ using the expression

$$\tau = \left\{ \pi r_e^2 c \int n_+(\boldsymbol{r}) n(\boldsymbol{r}) \gamma[n, \boldsymbol{\nabla} n] d\boldsymbol{r} \right\}^{-1}, \quad (3)$$

where r_e is the classical electron radius, and c is the speed of light. The electron enhancement factor γ accounts for the pile-up of electrons at the positron site [31]. The electron-positron correlation, i.e., the correlation potential V_{corr} and the enhancement factor γ, were treated within the generalized gradient approximation using the approach introduced by Barbiellini et al. [32]. With this approach, V_{corr} and γ are determined by the electron density n and its gradient $\boldsymbol{\nabla} n$ at the site of the positron.

The momentum distribution of the annihilating electron-positron pairs was calculated using the approach described in Refs. [33] and [34]. The contribution $\rho^{i,nl}$ from the i-th atom and a shell characterized by the principal and orbital quantum numbers n, l was calculated by the formula

$$\rho^{i,nl}(p) = 4\pi^2 r_e^2 c N^{i,nl} \gamma^{i,nl} \left| \int R_+^i R_-^{i,nl} B_l(pr) r^2 dr \right|^2, \quad (4)$$

where $N^{i,nl}$ denotes the number of electrons in the (n, l) shell, B_l is a spherical Bessel function, and R_+^i, $R_-^{i,nl}$ denote the radial part of the positron and electron wave functions. The symbol $\gamma^{i,nl}$ represents the state-dependent positron enhancement factor [34]. The momentum distribution of the annihilating electron-positron pairs was obtained by summing the partial contributions $\rho^{i,nl}(p)$ over all the occupied atomic sites and corresponding electron shells. Since the core electrons localized in atomic shells are practically not affected by crystal bonding and retain their atomic character, the present approach describes the high-momentum part of the momentum distribution ($p > 10 \times 10^{-3} m_0 c$) well, where the contribution of positrons annihilated by core electrons dominates. To mimic the effect of the finite resolution of the experimental setup, the theoretical momentum distribution curves were convolved with a Gaussian function with a full width at half maximum of $3.5 \times 10^{-3} m_0 c$. For the sake of comparison with the experiment, the calculated momentum
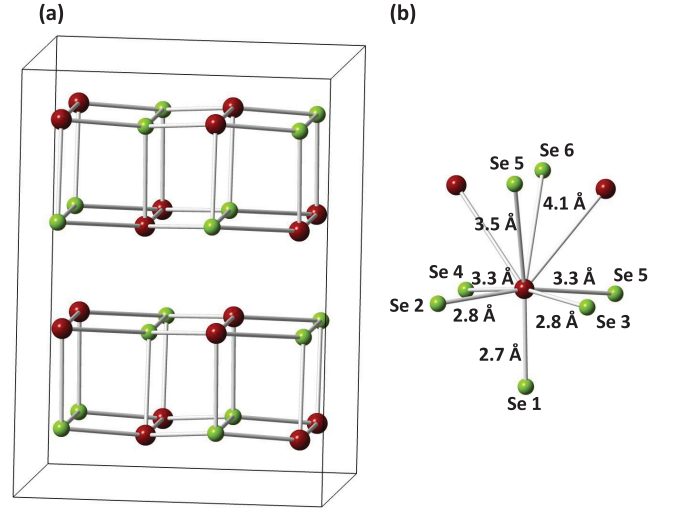

FIG. 1. (a) Structure of the SnSe *Pnma* phase; Sn and Se ions are indicated by red and green spheres, respectively. (b) Coordination of Sn ion. Interatomic distances between Sn and Se ions are denoted by labels.

distributions are presented as ratio curves related to the momentum distribution calculated for a perfect Al crystal.

Ab initio calculations were performed for the *Pnma* SnSe phase with orthorhombic structure ($a = 11.492$ Å, $b = 4.151$ Å, and $c = 4.442$ Å) [6], which represents the thermodynamic equilibrium phase at temperatures below ≈ 800 K [35,36]. Structure of the *Pnma* phase is shown in Fig. 1(a). Point defects were modeled using 512 atom-based supercells. The Brillouin-zone integration over the lowest-lying positron state described in Ref. [37] was used in calculations of the positron parameters for point defects to achieve a rapid convergence of the results with respect to the supercell size.

D. Transport measurements

The transport parameters include the electrical conductivity $\sigma(i \parallel b)$, the Hall coefficient $R_H(i \parallel b; B \parallel a)$, and the Seebeck coefficient $S(\Delta T \parallel b)$. These parameters were measured over a temperature range from 80 to 470 K. A conductive graphite adhesive was used to attach the current and voltage leads. The Hall effect and electrical conductivity were examined using a lock-in nanovoltmeter with a 29-Hz excitation and a static magnetic field of 0.6 T. To calculate the Hall concentration of the holes h, we used the simplified formula $R_H = 1/he$, which maintains correspondence with the literature. However, that might be disputable, at least for samples with ATs at approximately 700 K, where transport might be affected by the presence of heavy holes. The Seebeck coefficient was determined using the longitudinal steady-state technique with a temperature difference ranging from 3 to 3.5 K. The thermal gradients were measured with the aid of fine copper-constantan thermocouples.

E. Powder x-ray diffraction and sample orientation

X-ray diffraction (XRD) patterns (Cu Kα, $\lambda = 1.5418$ Å) were recorded for powdered samples using a D8 Advance

TABLE I. The bulk positron lifetime and the lifetimes of positrons trapped at various point defects obtained from *ab initio* calculations.

Positron state	τ (ps)
Bulk	217
V_{Sn}	308
V_{Se}	279
$V_{Sn} + V_{Se}$	358
$V_{Sn} + 2V_{Se}$	396
$V_{Sn} + 3V_{Se}$	431

FIG. 2. Configurations of vacancy clusters considered in *ab initio* calculations (a) $V_{Sn} + V_{Se}$, (b) $V_{Sn} + 2V_{Se}$, and (c) $V_{Sn} + 3V_{Se}$. Sn and Se ions are indicated by red and green spheres, respectively. Vacancies are denoted by open squares.

diffractometer (Bruker AXES, Germany) with a Bragg-Brentano $\theta - \theta$ goniometer (radius 217.5 mm) equipped with a Ni-beta filter and a LynxEye detector. Scans were performed at room temperature in the range from $10°$ to $90°$ (2Θ) in $0.01°$ steps with a counting time of 2 s per step. The lattice parameters were refined using the Le Bail method as implemented in the program FULLPROF [38]. Sample orientation was performed using electron backscatter diffraction (EBDS) on JEOL 733 equipped with an energy-dispersive x-ray analysis EBSD detector. EBSD data were analyzed with TSL OIM software.

III. RESULTS AND DISCUSSION

A. Positron annihilation spectroscopy

The lifetimes for the various positron states obtained from *ab initio* calculations are listed in Table I. The calculated bulk positron lifetime, i.e., the lifetime of free positrons delocalized in a perfect (defect-free) lattice of the *Pnma* phase of SnSe, is lifetime $\tau_B = 217$ ps. Both Sn vacancies (V_{Sn}) and Se vacancies (V_{Se}) represent deep trapping sites for positrons characterized by positron binding energies of 1.50 and 1.29 eV, respectively. The Sn vacancy exhibits a larger open volume than the Se vacancy, which is reflected by a longer lifetime of positrons trapped in V_{Sn} (308 ps) than positrons trapped in V_{Se} (279 ps). As shown in Fig. 1(b), Sn ion is surrounded by three Se ions in similar distance 2.7–2.8 Å. These ions are denoted in Fig. 1(b) as Se1, Se2, and Se3. Other Se ions [denoted in Fig. 1(b) as Se4–Se6] are located in significantly longer distance. V_{Se} was formed by removal of Se ion Se1, i.e., the nearest-neighbor Sn located in the distance of 2.7 Å. Two types of V_{Se} exist in the *Pnma* phase. First-type V_{Se} can be formed by removing the nearest-neighbor Se ion (Se1) located in the distance of 2.7 Å away from the Sn ion. Second-type V_{Se} is created by removal of Se2 or Se3 located in slightly longer distance of 2.8 Å away from the Sn ion. The difference in the calculated lifetimes of positrons trapped in these two types of V_{Se} does not exceed 0.5 ps and can therefore be neglected.

Complexes consisting of V_{Sn} associated with single or multiple V_{Se} were considered as well. Configuration of these complexes is shown in Fig. 2. $V_{Sn} + V_{Se}$ divacancy was formed by removal of the nearest-neighbor Se ion (Se1) located in the distance of 2.7 Å away from V_{Sn}, see Fig. 2(a). $V_{Sn} + 2V_{Se}$ vacancy cluster was created by removal of Se1 and Se2 ions located in distances 2.7 and 2.8 Å away from

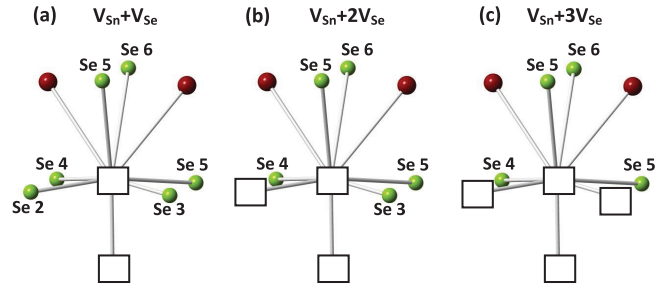V_{Sn}, see Fig. 2(b). $V_{Sn} + 3V_{Se}$ vacancy cluster was formed by removal of Se1, Se2, and Se3 ions, i.e., all three Se ions located in close distance of 2.7–2.8 Å from V_{Sn}, see Fig. 2(c). The calculated positron lifetimes for these vacancy clusters are listed in Table I as well. Table I shows that the lifetime of the trapped positrons increases with increasing open volume available in the defect.

The results of the LT experiments are summarized in Figs. 3–6. Figure 3 shows the development of the mean positron lifetime $\tau_{mean} = \sum_i \tau_i I_i$ with annealing temperature. The mean positron lifetime τ_{mean} is a robust parameter that is not influenced by mutual correlations between the fitting parameters. Hence, the behavior of τ_{mean} provides good insight into the development of defects in SnSe SCs. The dashed lines in Fig. 3 indicate the calculated lifetimes for various positron states. In the temperature range 300–600 K, τ_{mean} is, on the one hand, higher than the calculated bulk positron lifetime but, on the other hand, lower than the values calculated for mono-vacancies (V_{Se}, V_{Sn}). This indicates that some fraction of the positrons annihilates in the trapped state available at volume defects, while the remaining positrons are annihilated in the free state (i.e., not trapped at defects). With an AT increasing
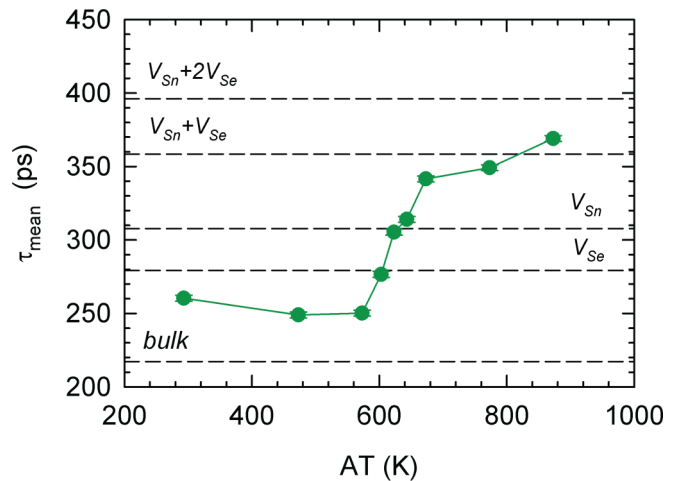

FIG. 3. The development of the mean positron lifetime τ_{mean} as a function of AT. The dashed lines show the calculated positron lifetimes for a perfect SnSe lattice (bulk) and for various types of defects.
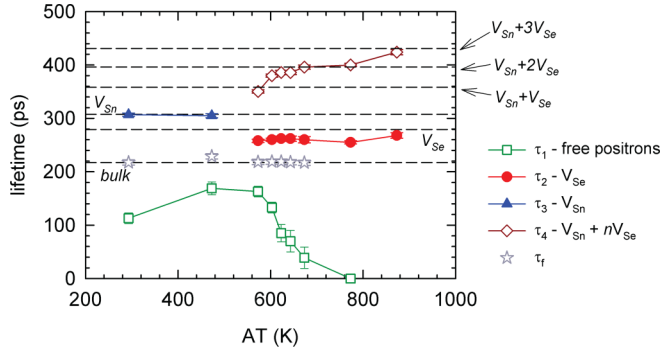
FIG. 4. The development of the lifetimes τ_i of the exponential components resolved in the LT spectra as a function of AT. The quantity τ_f calculated using Eq. (5) is plotted in the figure as well. The dashed lines show calculated lifetimes for various positron states.

above 300 K, τ_{mean} first slightly decreases towards the bulk value and shows a minimum at approximately 500 K. Thus, the lowest concentration of defects occurs at approximately 500 K. Above 600 K, the mean positron lifetime steeply increases even above the values calculated for V_{Se} and V_{Sn}, indicating a dramatic increase in the concentration of defects and the introduction of defects with a larger open volume than monovacancies.

More information about the defects can be obtained from the decomposition of the LT spectra into individual components. Figure 4 shows the development of the lifetimes τ_i of the exponential components resolved in the LT spectra with AT. The dashed lines in the figure again indicate the lifetimes calculated for various kinds of defects. The development of the corresponding intensities I_i of the components resolved in the LT spectra is plotted in Fig. 5 as a function of AT. Note that the intensities are always normalized so that $\sum_i I_i = 100\%$. In the AT region from 300 to 500 K, the LT spectra contain two components: (i) a short-lived component with lifetime τ_1 comes from free positrons annihilated in the delocalized state, not trapped at defects. Note that the lifetime τ_1 of the free-positron component becomes lower than the bulk lifetime τ_B (i.e., the lifetime of free positrons in a perfect lattice) because

of the presence of defects [39]. The second component is (ii) a longer component with lifetime τ_3 that can be attributed to positrons trapped at V_{Sn} since τ_3 agrees well with the calculated value for V_{Sn}. From the intensity behavior in Fig. 5, it becomes clear that Sn vacancy represents the dominant type of defect at an AT ≈ 300 K (note that a 293 K AT corresponds, in fact, to a nonannealed sample – see Sec. II A). With increasing AT, the concentration of V_{Sn} rapidly decreases, which leads to a pronounced drop in I_3. Above 600 K, the nature of the defects changes: the Sn-vacancy component cannot be resolved in LT spectra anymore, but two other components with lifetimes τ_2 and τ_4 appear. The component with lifetime $\tau_2 \approx 270$ ps can be attributed to positrons trapped at V_{Se}, as shown in Fig. 4. The longest component with lifetime $\tau_4 \geqslant 350$ ps comes obviously from positrons trapped at vacancy clusters, and its lifetime increases with increasing AT from ≈ 350 ps at 573 K to ≈ 430 ps at 873 K, indicating the growing size of the vacancy clusters. By comparison with the *ab initio* calculations, the latter component can be attributed to $V_{\mathrm{Sn}} + nV_{\mathrm{Se}}$ vacancy clusters where n varies between 1 and 3. From the development of the intensities in Fig. 5, one can conclude that the concentration of V_{Se} and $V_{\mathrm{Sn}} + nV_{\mathrm{Se}}$ increases with AT in the temperature range 600–800 K and becomes saturated above 800 K. Hence, V_{Se} and $V_{\mathrm{Sn}} + nV_{\mathrm{Se}}$ represent the dominant type of defect at elevated temperatures (AT > 600 K).

The concentrations of the point defects V_{Sn}, V_{Se}, and $V_{\mathrm{Sn}} + nV_{\mathrm{Se}}$ detected by LT spectroscopy can be calculated from the LT results using the simple trapping model (STM) [39]. The STM kinetic equations were derived assuming that the spatial distribution of the defects is uniform, no detrapping of positrons localized in the defects occurs, and only thermalized positrons can be trapped at defects. Within STM, the parameters of the exponential components τ_i, I_i are not fully independent but are interconnected so that the quantity

$$\tau_f = \left\{ \sum_i \frac{I_i}{\tau_i} \right\}^{-1} \qquad (5)$$

always equals the bulk positron lifetime, i.e., the lifetime of the free positrons in a perfect SnSe lattice: $\tau_f = \tau_B$. One can see in Fig. 4 that the quantity τ_f calculated using Eq. (5) agrees well with the calculated bulk lifetime for SnSe. It testifies that the assumptions of STM are fulfilled in the present case and can be used for the determination of defect concentrations.

The concentration of from the *i*-*th* kind of defect can be calculated from the equation [39]

$$c_i = \frac{I_i}{\nu_i} \left(\frac{1}{\tau_1} - \frac{1}{\tau_i} \right), \qquad (6)$$

where ν_i is the specific positron-trapping rate (cross section of positron trapping per unit concentration of defects) for the corresponding type of defect [39]. Since exact values of the specific positron-trapping rate for the vacancies in SnSe are unknown for V_{Se} and V_{Sn}, we used $\nu_V = 10^{14}$ at s^{-1}, representing an order of magnitude estimation of ν for neutral monovacancies in semiconductors [39]. The specific positron-trapping rate for small vacancy clusters (containing up to ten vacancies) is directly proportional to the number of vacancies in the cluster [39]. Hence, the specific positron-trapping rate
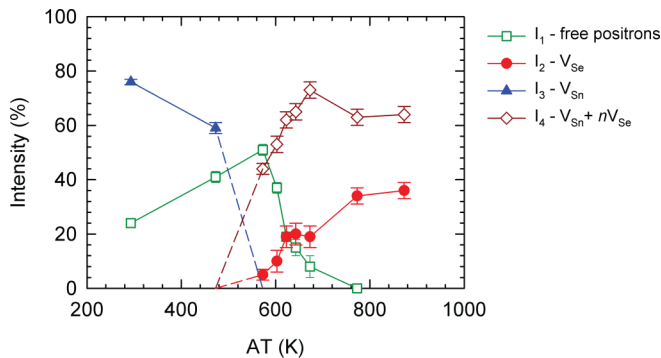

FIG. 5. The development of the relative intensities I_i of the exponential components resolved in the LT spectra as a function of AT. Dashed lines show extrapolation to zero intensity in case where the corresponding component could not be resolved in the spectrum.
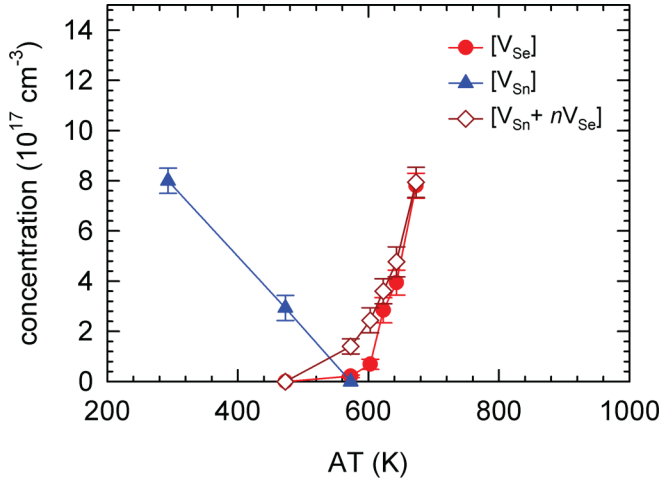
FIG. 6. The development of the concentrations of point defects detected by LT spectroscopy in SnSe SCs plotted as a function of AT.

for $V_{Sn} + nV_{Se}$ clusters was estimated as $(n + 1) \nu_V$. The concentrations of the point defects $[V_{Sn}]$, $[V_{Se}]$, and $[V_{Sn} + nV_{Se}]$ determined from the LT data are plotted in Fig. 6 as a function of AT. From inspection of the figure, it becomes clear that $[V_{Sn}]$ decreases with AT and diminishes at 600 K. Above this temperature, V_{Se} and $V_{Sn} + nV_{Se}$ appear, and their concentrations $[V_{Se}]$ and $[V_{Sn} + nV_{Se}]$ strongly increase with AT. Note that determination of the concentrations of defects from the LT data is possible only when the free-positron component τ_1 is resolved in LT spectra. At an $AT > 700$ K, saturated positron trapping occurs (i.e., the concentration of V_{Se} and $V_{Sn} + nV_{Se}$ becomes so high that virtually all positrons are annihilated in the trapped state), and the concentrations of defects cannot be determined anymore.

The calculated coincidence Doppler broadening ratio curves (related to Al) for a perfect (defect-free) SnSe crystal are plotted in Fig. 7(a). Positrons in SnSe are annihilated either by electrons belonging to Sn or Se. The partial contributions of positrons annihilated by Sn and Se electrons are plotted in Fig. 7 with dashed lines. The Se contribution is characterized by two peaks located at $p \approx 8 \times 10^{-3}$ and 18×10^{-3} m_0c. The prominent feature of the Sn contribution is a broad peak centered at $p \approx 12 \times 10^{-3}$ m_0c followed by a broad minimum at $p \approx 28 \times 10^{-3}$ m_0c. The fractions of positrons annihilated by Sn and Se electrons in a perfect SnSe crystal are comparable, namely, 53 and 47%.

The CDB ratio curves calculated for V_{Sn} and V_{Se} are plotted in Figs. 7(b) and 7(c). The Sn vacancy is surrounded by Se nearest neighbors. Hence, Se electrons annihilate the majority (63%) of the positrons trapped at V_{Sn}. In contrast, the Se vacancy is surrounded by Sn nearest neighbors, and the majority (67%) of positrons trapped at V_{Se} is, therefore, annihilated by Sn electrons.

The experimental CDB ratio curves for SnSe SCs are plotted in Fig. 8. The CDB ratio curves for reference samples of pure Sn and Se are plotted in the figure as well. The shapes of the high-momentum parts of the CDB ratio curve for pure Sn and Se are in good qualitative agreement with the calculated Sn and Se contributions. Note that the comparison of the experimental CDB curves for the Sn and Se reference
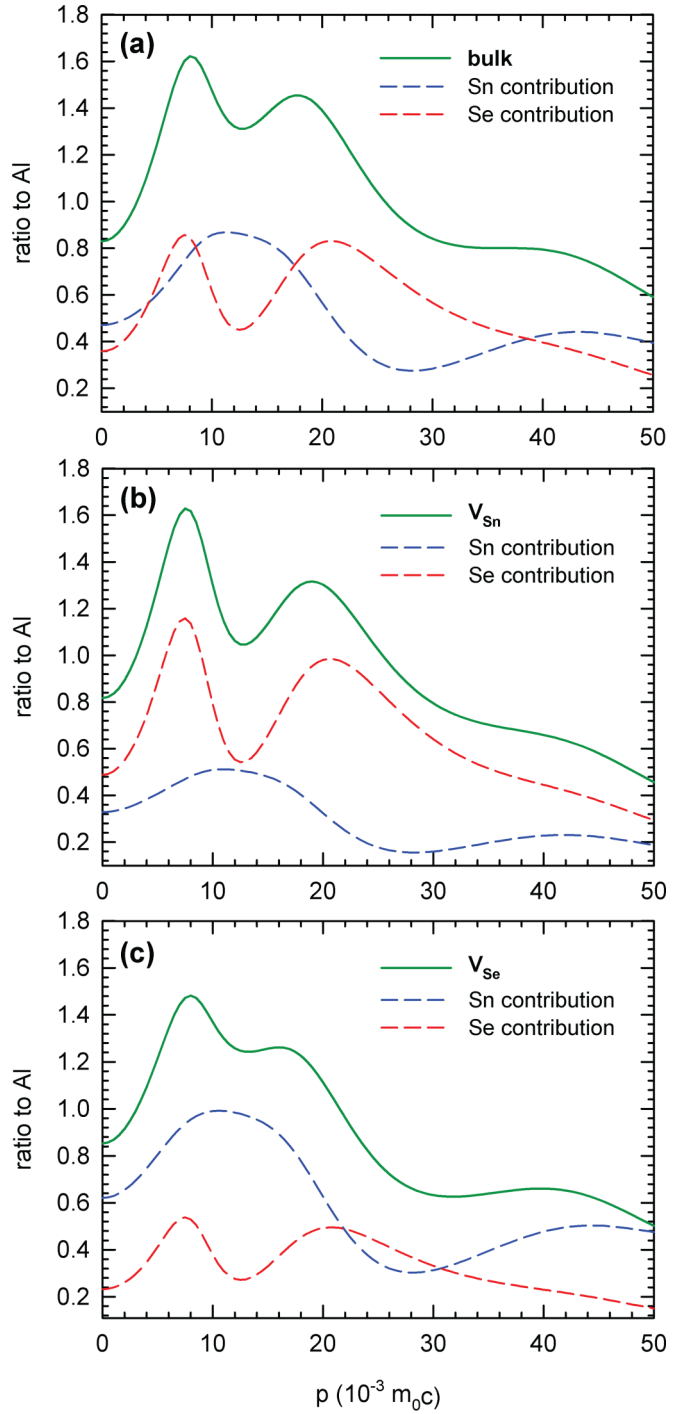

FIG. 7. The calculated CDB ratio curves (related to pure Al) for (a) the perfect SnSe crystal, (b) V_{Sn}, and (c) V_{Se}. Partial contributions of the positrons annihilated by Sn and Se electrons are plotted with dashed lines.

samples and the calculated Sn and Se contributions for a SnSe crystal is meaningful in the high-momentum region only with the dominating contribution of the core electrons, which retain their atomic character and are not influenced by crystal binding.

From inspection of Fig. 8, one can conclude that the CDB ratio curves for SnSe SCs for AT < 600 K exhibit similar fea-
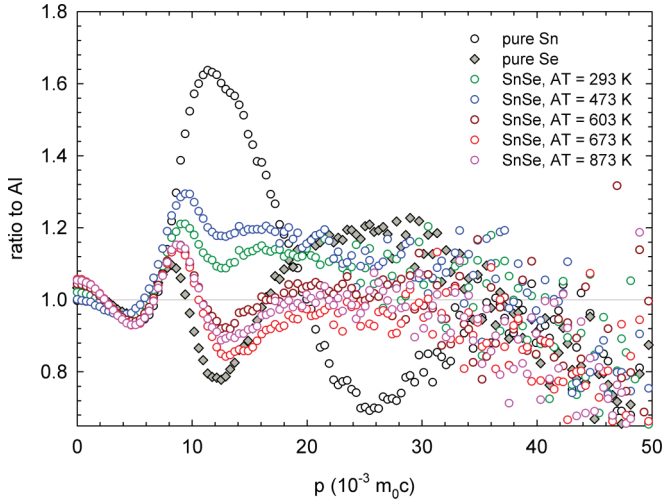
FIG. 8. Experimental CDB ratio curves (related to well-annealed pure Al) for SnSe SCs. The ratio curves for reference samples of pure Sn and Se are plotted in the figure as well.

tures, namely a peak at $p \approx 9 \times 10^{-3} m_0 c$ followed by a broad peak at higher momenta ($\sim 20 \times 10^{-3} m_0 c$). The CDB curve for AT = 473 K is only vertically shifted up with respect to the curve for AT = 293 K. This indicates that for AT < 600 K positrons were annihilated in similar chemical environment, i.e., the fraction of positrons annihilated in the vicinity of Sn and Se ions is comparable. In contrast, for AT $\geqslant$ 600 K the shape of the CDB curves significantly changes, indicating a change in the dominant type of defect. The calculated CDB ratio curves for various defects in SnSe are compared in Fig. 9. The CDB curves for all defects considered are characterized by the two characteristic peaks at $p \approx 8 \times 10^{-3}$ and $18 \times 10^{-3} m_0 c$, representing a contribution of positrons annihilated by Se electrons. For open volume defects, the CDB ratio curves generally decrease in the high-momentum region and increase for low momenta due to the localization of the positron wave function in the defect, which reduces its
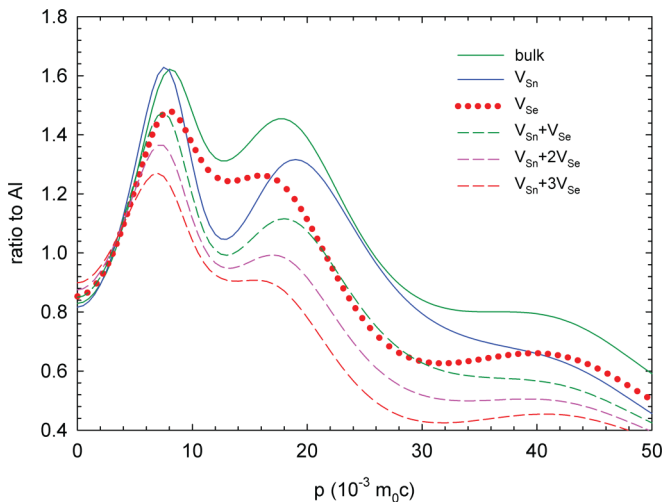

FIG. 9. Calculated CDB ratio curves (related to Al) for a perfect SnSe crystal and various point defects in SnSe.

overlap with core electron orbitals and thereby enhances the fraction of positrons annihilated by low-momentum valence electrons. Comparing Figs. 8 and 9, one can conclude that there is relatively good qualitative similarity between the CDB curves measured for SnSe SCs for AT < 600 K and the calculated CDB curve for V_{Sn}. This is in accordance with V_{Sn} representing the dominating type of defect for AT < 600 K. An enhancement of the experimental CDB curve in the high-momentum range caused by an increase in AT from 293 to 473 K corresponds well to a decrease in V_{Sn} concentration, i.e., a shift of the CDB ratio curve towards the curve for the bulk. For AT = 603 K and higher temperatures, the experimental CDB ratio curves drop in the high-momentum range (Fig. 8). This indicates the introduction of defects with a larger open volume than the open volume of V_{Sn}, which is consistent with the creation of $V_{Sn} + nV_{Se}$ clusters, cf. Fig. 6. Indeed, the shape of the experimental CDB ratio curves for AT $\geqslant$ 600 K is in good qualitative agreement with the calculated curves for the $V_{Sn} + nV_{Se}$ clusters. The drop in the experimental CDB curves in the high-momentum range is more pronounced when AT increases from 603 to 873 K (see Fig. 8). This is in accordance with the increasing concentration of $V_{Sn} + nV_{Se}$ clusters. Hence, the CDB investigations support the picture that the Sn vacancy represents the dominating type of defect at AT < 600 K, while at higher temperatures (AT $\geqslant$ 600 K) the dominating defect changes to V_{Se} and $V_{Sn} + nV_{Se}$.

An enhanced concentration of Sn-poor domains as large as several nanometers, interpreted as V_{Sn}, was reported in Ref. [21] for a polycrystalline material prepared by mechanical alloying and compacted using spark plasma sintering (SPS). The SPS process is fast enough to facilitate the freezing of this type of defect. In fact, these defects are not thermodynamically stable at lower temperatures and most likely disappear upon thermal cycling. Moreover, the large understoichiometry of Sn (up to x = 0.1 for $Sn_{1-x}Se$) investigated in Ref. [21] would definitely lead to a mixture of SnSe and $SnSe_2$ in the equilibrium state [25]. The PAS results suggest another scenario for the near-equilibrium state. In contrast to Ref. [21], we observed a decrease in isolated V_{Sn} upon increasing AT and their complete depletion between 500 and 600 K AT (see Fig. 6); instead of V_{Sn}, V_{Se} and $V_{Sn} + nV_{Se}$ vacancy complexes are formed above 520 K. Although very rarely, $V_{Sn} + 2V_{Se}$ were observed using high resolution scanning transmission electron microscopy (HR-STEM) [24]. Based on the DFT calculations, it has been reported that both V_{Se} and $V_{Sn} + 2V_{Se}$ produce only localized electrons and do not contribute to band transport in SnSe [24]. While V_{Se} can behave as both a donor and an acceptor depending on the Fermi level [23], the complex defects ($V_{Sn} + nV_{Se}$) tend to be acceptors. This is indicated by the transport measurements (increase in the hole concentration) presented in Sec. III B. Note that according to the PAS results, no isolated V_{Sn} are available in the SnSe structure at elevated temperatures (above 600 K) in contrast to the conclusions of previous publications, e.g., Refs. [15] and [24]. As discussed below, the formation of complex defects is accompanied by the formation of $SnSe_2$ precipitates. Thus, the increase in the hole concentration can be partially attributed to charge (electron) transfer from SnSe to $SnSe_2$, as suggested in Ref. [25]. Note that such large complex defects like $V_{Sn} + nV_{Se}$ might mimic the energy filtering

of FC generally provided by ionized point defects at lower temperatures [40]. This would prevent any abrupt decrease in the Seebeck coefficient or the power function (PF) with increasing FC concentration (see discussion in Sec. III B.). Furthermore, $V_{Sn} + nV_{Se}$ can modify the band structure in favor of higher effective masses [21]. The presence of such complex vacancies in the lattice effectively decreases the thermal conductivity of crystals. The complex vacancies naturally explain the pronounced anharmonicity and softening of phonons [41,42]. The formation of complex vacancies also triggers the formation of $SnSe_2$ at elevated temperatures, namely, the V_{Se}/V_{Sn} ratio in complexes ranges between 1 and 3, which drives the system towards the formation of a Se-rich phase. This implies that the SnSe matrix prefers Se understoichiometry at elevated temperatures and that there is a strong tendency for Se segregation. Note that this process could also lead to the formation of a high concentration of Se interstitials in an intermediate state, as observed in Ref. [22]. On the other hand, below 500 K, the SnSe matrix prefers Se overstoichiometry, which is achieved by the formation of V_{Sn} (see Fig. 4).

We suggest that the formation of V_{Se} and $V_{Sn} + nV_{Se}$ at elevated temperatures above 600 K and decomposition into $SnSe_2$ and Sn phase is the reason for the discrepancy observed between the TE performances of SC and PC SnSe materials. Namely, vacancies and complex vacancies can diffuse and annihilate on the grain boundaries in a PC, but they survive within the bulk of an SC. Similarly, second-phase particles may segregate on grain boundaries within a PC, while in an SC, they remain as nanoinclusions. Indeed, the presence of Sn nanoinclusions was reported in K-doped SnSe [43]. We think that any effect of other intrinsic defects (Sn_{Se}, Se_{Sn}, Sn_i,) is not manifested until one approaches higher temperatures (≈ 600 K) due to the high formation energies in that regime [23]. We discuss this issue in Sec. III B.

B. Transport properties

The Hall FC concentration h as a function of AT is shown in Fig. 10. We used the simplified formula $h = 1/R_H e$, with R_H being the Hall coefficient. The lowest hole concentration is achieved by annealing in the range from 473 to 573 K. This is in accordance with the lowest concentration of vacancies measured by PAS. Note that the Sn vacancy is the dominant type of defect in this temperature range. For higher temperatures (AT > 600 K), we observe a steep increase in the hole concentration of an order of magnitude with a maximum at 673 K. Note that this increase is ascribed to the formation of V_{Sn} with a formation energy of 0.67 eV and not the thermal activation in, i.e., ionization [15,21]. In contrast, the PAS results suggest that p-type conductivity is not due to V_{Sn} but due to the introduction of ($V_{Sn} + nV_{Se}$) or V_{Se} (see Fig. 6). We observe a steep increase in the hole concentration for sample 673 K AT passing from 300 to 400 K, which indicates thermal excitations (see Fig. 10). This contradicts the results of the DFT calculations in [24] in two ways. First, it is declared in Ref. [24] that V_{Se} and ($V_{Sn} + 2V_{Se}$) produce just electrons, not holes. Second, according to calculations [24], electrons are localized, i.e., they are not involved in band transport. The decrease in Hall concentration above 673 K AT is less clear. A
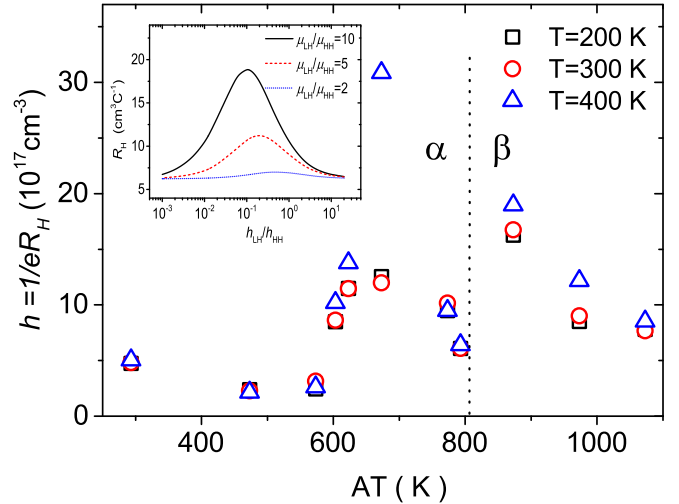

FIG. 10. Hall concentration h of holes of SnSe as a function of AT for three temperatures. Note the significant increase in the hole concentration between 300 and 400 K for 673 K AT, which is indicative of thermal excitation. The dotted line represents the $\alpha \rightarrow \beta$ transition temperature (≈ 810 K) of SnSe. The inset documents the eventual impact of heavy holes (HH) if combined with light holes (LH) in terms of carrier mobility. The curves are calculated using $R_H = \frac{1}{|e|} \frac{(h_{HH} \mu_{HH}^2 + h_{LH} \mu_{LH}^2)}{(h_{HH} \mu_{HH} + h_{LH} \mu_{LH})^2}$, where h and μ are the respective hole concentration and mobility.

plausible explanation involves the formation of a defect band that contributes to transport itself or resonates with the valence band [21]. We assume that the concentration of defects is high enough to realize a slight overlap, which implies heavy carriers. This assumption is strongly corroborated by the Pisarenko plot which will be discussed later. A population of heavy holes can explain the decrease in Hall concentration (see inset of Fig. 10). Thus, we must admit that the simplified formula $h = 1/R_H e$ does not correctly reflect the reality at AT $\geqslant 700$ K. Finally, the effect of charge transfer from SnSe to $SnSe_2$ can play a certain role and eventually produce holes, as mentioned in the Introduction [25]. However, we are not able to address that issue at this moment.

The Hall mobility μ_H (Fig. 11) is comparable in magnitude with the data published in Ref. [18]. In accordance with the PAS results, the mobility of FC increases with a decreasing concentration of V_{Sn} and peaks around AT ≈ 600 K, i.e., close to the temperature where the lowest concentration of defects is found. An interesting transient drop in FC mobility (and partially in the PF) appears at an AT of approximately 773 K (Fig. 11). This suggests that the concentration of defects (disorder) is higher at 773 than at 793 K, which is a temperature on the verge of the $\alpha \rightarrow \beta$ transformation. Indeed, the concentration of $V_{Sn} + nV_{Se}$ clusters is lower at 793 than at 773 K according to PAS (see a drop of I_4 in Fig. 5). On the other hand, this can suggest that the transition temperature is lower than 800 K, as reported in Ref. [44]. We note that the positions of the Sn and Se atoms vary abruptly well below 800 K [6,45].

The power factor $PF = \sigma S^2$ (σ and S are electrical conductivity and Seebeck coefficient, respectively) of SnSe as a function of AT is depicted in Fig. 12. The material annealed at 673
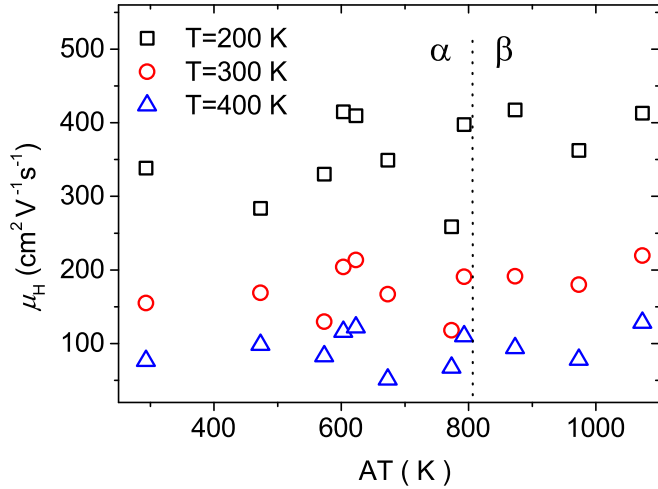
FIG. 11. Hall mobility μ_H of SnSe as a function of AT for three temperatures. The dotted line represents the $\alpha \rightarrow \beta$ transition temperature ($\approx$810 K) of SnSe.

K shows a high PF $\approx 2\,\mathrm{mWm^{-1}\,K^{-2}}$ at a rather low temperature of 200 K. With respect to the AT, the PF maximum coincides with the domination of $V_{Sn} + nV_{Se}$ clusters and V_{Se}. It is obvious from Fig. 6 that the concentrations of V_{Se} and $V_{Sn} + nV_{Se}$ markedly increase with an AT approaching 673 K. The PAS data in Figs. 4 and 5 testify that the concentration of V_{Se} further increases and n becomes larger for $V_{Sn} + nV_{Se}$ clusters above 673 K. Note that concentrations of both V_{Se} and $V_{Sn} + nV_{Se}$ also remain high in β-SnSe, i.e., above $\sim$800 K. Admittedly, the $\beta \rightarrow \alpha$ crossover during the quenching of the samples can affect the concentration of these defects. Thus, the results for the samples annealed above 800 K should be considered with caution. For an AT between 573 and 673 K, the FC concentration increases by an order of magnitude and the Seebeck coefficient decreases by $\approx$15%. This indicates extraordinary behavior, as discussed in the next section. The decrease in mobility above 673 K is due to both an increase in
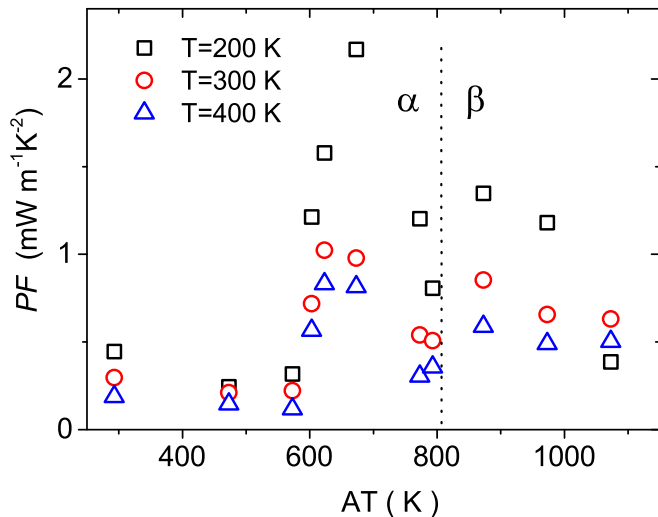

FIG. 12. PF as a function of AT. The dotted line represents the $\alpha \rightarrow \beta$ transition temperature ($\approx$810 K) of SnSe.
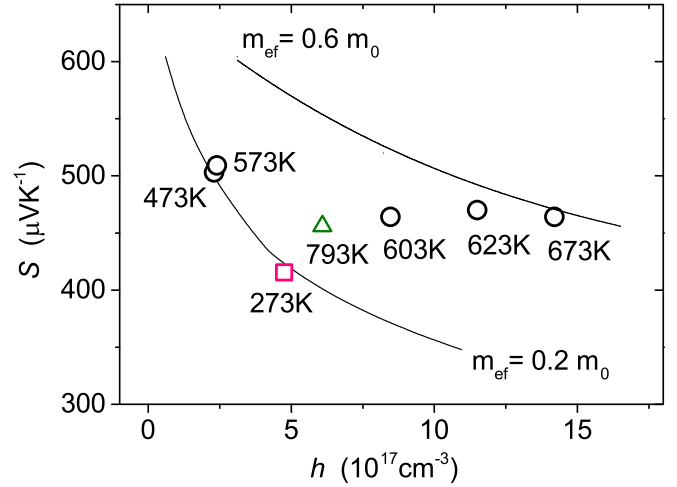

FIG. 13. The Seebeck coefficient S as a function of the Hall concentration of holes (Pisarenko plot) for various ATs (not shown are the samples annealed above the $\alpha \rightarrow \beta$ transition temperature $\approx$800 K). The solid lines are fits using a single parabolic model assuming scattering of FCs by acoustic phonons. The sample annealed at 793 K (green triangle) is on the verge of the $\alpha \rightarrow \beta$ transition. The red square represents the standard (nonannealed) sample. The values were measured at $T = 200$ K.

the concentration of defects and the presence of heavy holes. Interestingly, both V_{Se} and vacancy clusters do not induce a dramatic decrease in mobility for an AT of 673 K (Fig. 11).

Figure 13 shows the Seebeck coefficient as a function of the hole concentration (Pisarenko plot) for various ATs. The solid lines are fits to a single parabolic model assuming scattering of FCs by acoustic phonons [40]. A marked virtual increase in the density of states (DOS) effective mass of FC was observed when AT increased from 473 to 673 K. It is obvious that this violates the model. The results coincide with the outputs resulting from PAS and transport parameter analysis, i.e., with increasing defect concentration, which effectively leads to an increase in effective mass [21]. In the literature, such extraordinary behavior has been attributed to a steep variation of the effective mass [17,21,46], multivalley transport [25], or the quasi-2D thermoelectricity of SnSe [19,20]. We propose another idea that can help in explaining the extraordinary properties of SnSe: the extra energy filtering of the FCs by the V_{Se} defects or clusters of $V_{Sn} + nV_{Se}$ that mimic the increase in the DOS effective mass and the Seebeck coefficient. The virtual increase in the DOS effective mass can be induced by a shift of the scattering mechanism of the FCs towards a more energetically dependent one. For example, the scattering by ionized impurities produces a much higher Seebeck coefficient than scattering by acoustic phonons for the same FC concentration. Hence, one obtains a virtually larger DOS effective mass of FCs. The scattering of FCs by ionized V_{Se} up to unusually high temperatures was recently suggested for Bi_2Se_3 in Ref. [40]. An increasing concentration of V_{Se} and clusters might be the reason for this phenomenon in SnSe. In comparison with single vacancies, larger defects (clusters $V_{Sn} + nV_{Se}$) may provide more-pronounced energy filtering. It has to be noted that the DOS effective mass $m_{ef} = 0.2m_0$ is lower than that reported in the literature (Fig. 13). For samples
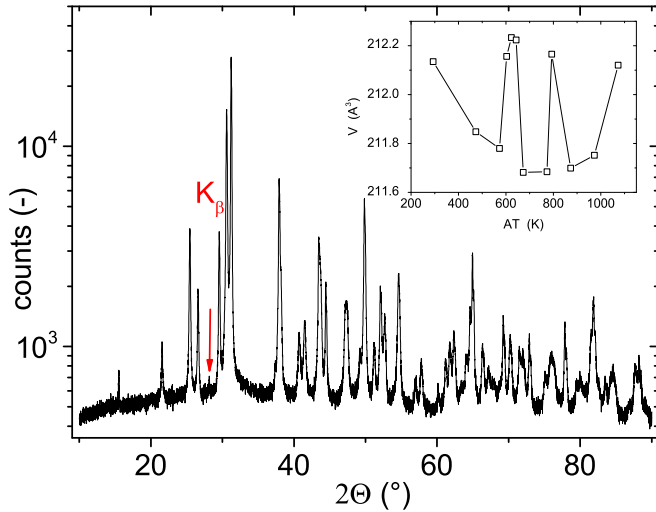
FIG. 14. A typical PXRD pattern of a powdered SnSe single crystal. No traces of foreign phases are detectable. The red arrow shows the K_β reflection. The inset documents the variation of UCV with AT. The maximum deviation of the UCV is $\pm 0.1 A^3$.

with $n \sim 10^{17} cm^{-3}$ at 200 K, one edge closest subband of light holes is involved in transport, which results in a lower DOS and effective mass [4]. The DOS effective mass of the upper valence band is $\approx 0.5 m_0$ based on DFT calculations [4]. On the other hand, the upper-band DOS effective mass derived from Shubnikov–de Haas (SdH) effect is $m_{ef} \approx 0.3 m_0$ [25]. From photoemission spectra, one obtains $\approx 0.35 m_0$ [47]. In addition, the defect-derived states can resonate with band states and enhance the DOS [21]. Contrary to other papers, the present paper deals with equilibrium-close state of SnSe, which implies lower (equilibrium) defect concentration. Although the Hall concentrations may be biased they indicate the overall trend correctly.

C. Powder x-ray diffraction

Powder x-ray diffraction (PXRD) was employed for characterization of the phase purity and determination of the lattice parameters of the prepared SCs. Before the measurements, the SCs were powdered. No foreign phases were observed at any AT. An example of the PXRD pattern is depicted in Fig. 14. The unit-cell volume as a function of AT is shown in the inset. All the lattice parameters (a, b, c) show similar behavior. The evolution of the unit-cell volume (UCV) with AT reflects the AT dependence of the concentration of intrinsic defects as discussed above. One can assume that vacancies induce expansion of the structure due to the failure of bonding. Hence, the UCV reaches a local minimum for the sample annealed at 573 K, where the concentration of defects reaches a minimum. Furthermore, the UCV increases steeply with increasing concentration of defects, but the UCV drops to an absolute minimum at AT = 673 K, where the concentration of vacancies is much higher. We assume that the concentration of vacancies becomes so large that the lattice somewhat collapses or the concentration of vacancy clusters decreases.

It is worth mentioning that the large concentration of V_{Se} and clusters $V_{Sn} + nV_{Se}$ implies that SnSe prefers a Se-poor composition. The spare Se reacts with SnSe to produce $SnSe_2$ with a layered structure comprising Van der Waals (VdW)-bonded triplet layers Se–Sn–Se [25]. It is assumed that $SnSe_2$ can be embedded in the form of very thin layers (a few triplets) between the VdW-bonded doublets of SnSe that are not detectable by PXRD. This point requires further investigation using high-resolution x-ray diffraction techniques.

IV. CONCLUSIONS

The present study showed that single-crystalline SnSe in an equilibrium-close state has a pronounced defect structure at all temperatures that is governed by vacancies. Tin vacancies V_{Sn} dominate at low temperatures ($T \leqslant 500$ K), while selenium vacancies V_{Se} and clusters $V_{Sn} + nV_{Se}$ dominate at higher temperatures. This implies that SnSe prefers a Se-rich composition at low temperatures and a Se-poor composition at higher temperatures ($T \geqslant 600$ K), i.e., its actual stoichiometry varies with temperature. Furthermore, the spare Se that is liberated with increasing temperature reacts with SnSe to produce *in situ* $SnSe_2$ in equilibrium. V_{Se} and primary clusters $V_{Sn} + nV_{Se}$ play an important role in transport in favor of the excellent TE properties. This applies for both the α- and β phase. First, all the defects decrease the thermal conductivity due to the introduction of extra scattering and strong anharmonicity. Second, the defects help to increase the PF of the material due to a local increase in the DOS effective mass or extra energy-dependent scattering.

The occurrence of V_{Se} and clusters $V_{Sn} + nV_{Se}$ is connected with an increase in the DOS effective mass. This increase could be real or virtual. Namely, it can be induced by a shift of the scattering mechanism of FCs towards a more energetically dependent mechanism, which is connected with a higher Seebeck coefficient, than for scattering by acoustic phonons for the same FC concentration. Hence, a virtually larger DOS effective mass of FCs is obtained. The occurrence of V_{Se} and vacancy clusters might be the reason for this phenomenon.

The present study suggests an explanation for why the TE properties of SCs are always much better than the TE properties of PCs. We hypothesize that the concentration of defects remains much higher in SCs than in PCs. The reason might be that such defects (being created due to the variation in the equilibrium stoichiometry with temperature) can accumulate at grain boundaries in PC while staying within the bulk in SC. The defects formed within the SC bulk keep their nanoscopic nature; hence, they can dissolve and precipitate upon cycling repeatedly. Note that the accumulation at grain boundaries leads to an effective annihilation of defects in the case of vacancies. This process decreases the actual concentration of vacancies within the structure and effectively increases the thermal conductivity of crystallites. Additionally, such annihilation of vacancies kills the eventual effective mass enhancement of the FC or an extra energy-dependent scattering of electrons. The accumulation of foreign phase $SnSe_2$ at the grain boundary hinders electronic transport in the case of PCs. On the other hand, nanoscopic inclusions of $SnSe_2$ may be beneficial for TE properties in the case of single crystals.

[1] G. S. Nolas, J. Sharp, and H. J. Goldsmid, *Thermoelectrics, Basic Principles and New Materials Developments* (Springer, Berlin, 2001), p. 128.

[2] L.-D. Zhao, S.-H. Lo, Y. Zhang, H. Sun, G. Tan, C. Uher, C. Wolverton, V. P. Dravid, and M. G. Kanatzidis, Ultralow thermal conductivity and high thermoelectric figure of merit in SnSe crystals, Nature (London) **508**, 373 (2014).

[3] L.-D. Zhao, G. Tan, S. Hao, J. He, Y. Pei, H. Chi, H. Wang, S. Gong, H. Xu, V. P. Dravid, C. Uher, G. J. Snyder, C. Wolverton, and M. G. Kanatzidis, Ultrahigh power factor and thermoelectric performance in hole-doped single-crystal SnSe, Science **351**, 141 (2016).

[4] K. Peng, B. Zhang, H. Wu, X. Cao, A. Li, D. Yang, X. Lu, G. Wang, X. Han, C. Uher, and X. Zhou, Ultra-high average figure of merit in synergistic band engineered $Sn_xNa_{1-x}Se_{0.9}S_{0.1}$ single crystals, Mater. Today **21**, 501 (2017).

[5] S. Sassi, C. Candolfi, J.-B. Vaney, V. Ohordniichuk, P. Masschelein, A. Dausher, and B. Lenoir, Assessment of the thermoelectric performance of polycrystalline p-type SnSe, Appl. Phys. Lett. **104**, 212105 (2014).

[6] M. Sist, J. Zhang, and B. Brummerstedt Iversen, Crystal structure and phase transition of thermoelectric SnSe, Acta Crystallogr., Sect. B: Struct. Sci., Cryst. Eng. Mater. **72**, 310 (2016).

[7] D. Ibrahim, J.-B. Vaney, S. Sassi, C. Candolfi, V. Ohordniichuk, P. Levinsky, C. Semprimoschning, A. Dausher, and B. Lenoir, Reinvestigation of the thermal properties of single-crystalline SnSe, Appl. Phys. Lett. **110**, 032103 (2017).

[8] Ch.-L. Chen, H. Wang, Y.-Y. Chen, T. Day, and G. J. Snyder, Thermoelectric properties of p-type polycrystalline SnSe doped with Ag, J. Mater. Chem. A **2**, 11171 (2014).

[9] A. J. Hong, L. Li, H. X. Zhu, Z. B. Yan, J.-M. Liu, and Z. F. Ren, Optimizing the thermoelectric performance of low-temperature SnSe compounds by electronic structure design, J. Mater. Chem. A **3**, 13365 (2015).

[10] Q. Zhang, E. K. Chere, J. Sun, F. Cao, K. Dahal, S. Chen, G. Chen, and Z. Ren, Studies on thermoelectric properties of n-type polycrystalline $SnSe_{1-x}S_x$ by iodine doping, Adv. Energy. Mater. **5**, 1500360 (2015).

[11] J. Gao and G. Xu, Thermoelectric performance of polycrystalline $Sn_{1-x}Cu_xSe (x = 0-0.03)$ prepared by high pressure method, Intermetallics **89**, 40 (2017).

[12] V. Kucek, T. Plechacek, P. Janicek, P. Ruleova, L. Benes, J. Navratil and C. Drasar, Thermoelectric properties of Tl-doped SnSe: A hint of phononic structure, J. Electron. Mater. **45**, 2943 (2016).

[13] Z.-H. Ge, D. Song, X. Chong, F. Zheng, L. Jin, X. Qian, L. Zheng, R. E. Dunin-Borkowski, P. Qin, J. Feng, and L.-D. Zhao, Boosting the thermoelectric performance of (Na,K)-codoped polycrystalline SnSe by synergistic tailoring of the band structure and atomic-scale defect phonon scattering, J. Am. Chem. Soc. **139**, 9714 (2017).

[14] Ch. Chang, Q. Tan, Y. Pei, Y. Xiao, X. Zhang, Y.-X. Chen, L. Zheng, S. Gong, J.-F. Li, J. He and L.-D. Zhao, Raising thermoelectric performance of n-type SnSe via Br doping and Pb alloying, RSC Adv. **6**, 98216 (2016).

[15] A. Dewandre, O. Hellman, S. Bhattacharya, A. H. Romero, G. K. H. Madsen, and M. J. Verstraete, Two-Step Phase Transition in SnSe and the Origins of Its High Power Factor from First Principles, Phys. Rev. Lett. **117**, 276601 (2016).

[16] J. Yang, G. Zhang, G. Yang, Ch. Wang, and Y. X. Wang, Outstanding thermoelectric performances for both p- and n-type SnSe from first-principles study, J. Alloys Compd. **644**, 615 (2015).

[17] Q. Lu, M. Wu, D. Wu, Ch. Chang, Y.-P. Guo, Ch.-S. Zhou, W. Li, X.-M. Ma, G. Wang, L.-D. Zhao, L. Huang, Ch. Liu, and J. He, Unexpected Large Hole Effective Masses in SnSe Revealed by Angle-Resolved Photoemission Spectroscopy, Phys. Rev. Lett. **119**, 116401 (2017).

[18] A. T. Duong, V. Q. Nguyen, G. Duvjir, V. T. Duong, S. Kwon, J. Y. Song, J. K. Lee, J. E. Lee, S. S. Park, T. Min, J. Lee, J. Kim, and S. Cho, Achieving. ZT = 2.2 with Bi-doped n-type SnSe single crystals, Nat. Commun. **7**, 13713 (2016).

[19] Ch. Chang, M. Wu, D. He, Y. Pei, Ch.-F. Wu, X. Wu, H. Yu, F. Zhu, K. Wang, Y. Chen, L. Huang, J.-F. Li, J. He, and L.-D. Zhao, 3D charge and 2D phonon transports leading to high out-of-plane ZT in n-type SnSe crystals, Science **360**, 778 (2018).

[20] V. Tayari, B. V. Senkovskiy, D. Rybkovskiy, N. Ehlen, A. Fedorov, C.-Y. Chen, J. Avila, M. Asensio, A. Perucchi, P. di Pietro, L. Yashina, I. Fakih, N. Hemsworth, M. Petrescu, G. Gervais, A. Grueneis, and T. Szkopek, Quasi-two-dimensional thermoelectricity in SnSe, Phys. Rev. B **97**, 045424 (2018).

[21] W. Wei, Ch. Chang, T. Yang, J. Liu, H. Tang, J. Zhang, Y. Li, F. Xu, Z. Zhang, J. F. Li, and G. Tang, Achieving high thermoelectric figure of merit in polycrystalline SnSe via introducing Sn vacancies, J. Am. Chem. Soc. **140**, 499 (2018).

[22] D. Wu, L. Wu, D. He, L.-D. Zhao, W. Li, M. Wu, M. Jin, J. Xu, J. Jiang, L. Huang, Y. Zhu, M. G. Kanatzidis, and J. He, Direct observation of vast off-stoichiometric defects in single crystalline SnSe, Nano Energy **35**, 321 (2017).

[23] Y. Huang, Ch. Wang, X. Chen, D. Zhou, J. Du, S. Wang, and L. Ning, First-principles study on intrinsic defects of SnSe, RSC Adv. **7**, 27612 (2017).

[24] G. Duvjir, T. Min, T. T. Ly, T. Kim, A.-T. Duong, S. Cho, S. H. Rhim, J. Lee, and J. Kim, Origin of p-type characteristics in a SnSe single crystal, Appl. Phys. Lett. **110**, 262106 (2017).

[25] Z. Wang, C. Fan, Z. Shen, Ch. Hua, Q. Hu, F. Sheng, Y. Lu, H. Fang, Z. Qiu, J. Lu, Z. Liu, W. Liu, Y. Huang, Z.-A. Xu, D. W. Shen, and Y. Zheng, Defects controlled hole doping and multivalley transport in SnSe single crystals, Nat. Commun. **9**, 47 (2018).

[26] R. Krause-Rehberg and H. Leipner, *Positron Annihilation in Semiconductors* (Springer-Verlag, Berlin, 1999).

[27] P. Asoka-Kumar, M. Alatalo, V. J. Ghosh, A. C. Kruseman, B. Nielsen, and K. G. Lynn, Increased Elemental Specificity of Positron Annihilation Spectra, Phys. Rev. Lett. **77**, 2097 (1996).

[28] F. Becvar, J. Cizek, I. Prochazka, and J. Janotova, The asset of ultra-fast digitizers for positron-lifetime spectroscopy, Nucl. Instrum. Methods Phys. Res., Sect. A **539**, 372 (2005).

[29] I. Prochazka, I. Novotny, and F. Becvar, Application of maximum-likelihood method to decomposition of positron-lifetime spectra to finite number of components, Mater. Sci. Forum. **255-257**, 772 (1997).

[30] J. Cizek, M. Vlcek, and I. Prochazka, Digital spectrometer for coincidence measurement of Doppler broadening of positron annihilation radiation, Nucl. Instrum. Methods Phys. Res., Sect. A **623**, 982 (2010).

[31] M. J. Puska and R. M. Nieminen, Theory of positrons in solids and on solid surfaces, Rev. Mod. Phys. **66**, 841 (1994).

[32] B. Barbiellini, M. J. Puska, T. Korhonen, A. Harju, T. Torsti, and R. M. Nieminen, Calculation of positron states and annihilation in solids: A density-gradient-correction scheme, Phys. Rev. B **53**, 16201 (1996).

[33] M. Alatalo, B. Barbiellini, M. Hakala, H. Kauppinen, T. Korhonen, M. J. Puska, K. Saarinen, P. Hautojärvi, and R. M. Nieminen, Theoretical and experimental study of positron annihilation with core electrons in solids, Phys. Rev. B **54**, 2397 (1996).

[34] J. Kuriplach, A. L. Morales, C. Dauwe, D. Segers, and M. Sob, Vacancies and vacancy-oxygen complexes in silicon: Positron annihilation with core electrons, Phys. Rev. B **58**, 10475 (1998).

[35] H. Wiedemeier and F. J. Csillag, The thermal expansion and high temperature transformation of SnS and SnSe, Z. Kristallogr. **149**, 17 (1979).

[36] K. Adouby, C. Perez-Vicente, J. C. Jumas, R. Fourcade, and A. A. Toure, Structure and temperature transformation of SnSe. Stabilization of a new cubic phase Sn4Bi2Se7, Z. Kristallogr. **213**, 343 (1998).

[37] T. Korhonen, M. J. Puska, and R. M. Nieminen, First-principles calculation of positron annihilation characteristics at metal vacancies, Phys. Rev. B **54**, 15016 (1996).

[38] https://www.ill.eu/sites/fullprof/.

[39] R. M. Nieminen and J. Laakkonen, Positron trapping rate into vacancy clusters, Appl. Phys. **20**, 181 (1979).

[40] P. Cermak, P. Ruleova, V. Holy, J. Prokleska, V. Kucek, K. Palka, L. Benes, and C. Drasar, Thermoelectric and magnetic properties of Cr-doped single crystal Bi_2Se_3 - Search for energy filtering, J. Solid. State. Chem. **258**, 768 (2018).

[41] J. M. Skelton, L. A. Burton, S. C. Parker, and A. Walsh, Anharmonicity in the High-Temperature Cmcm Phase of SnSe: Soft Modes and Three-Phonon Interactions, Phys. Rev. Lett. **117**, 075502 (2016).

[42] D. Bansal, J. Hong, Ch. W. Li, A. F. May, W. Porter, M. Y. Hu, D. L. Abernathy, and O. Delaire, Phonon anharmonicity and negative thermal expansion in SnSe, Phys. Rev. B **94**, 054307 (2016).

[43] Y. X. Chen, Z.-H. Ge, M. Yin, D. Feng, X.-Q. Huang, W. Zhao, and J. He, Understanding of the extremely low thermal conductivity in high-performance polycrystalline SnSe through potassium doping, Adv. Funct. Mater. **26**, 6836 (2016).

[44] F. Serrano-Sánchez, N. M. Nemes, O. J. Dura, M. T. Fernandez-Diaz, J. L. Martínez, and J. A. Alonso, Structural phase transition in polycrystalline SnSe: A neutron diffraction study in correlation with thermoelectric properties, J. Appl. Cryst. **49**, 2138 (2016).

[45] T. Chattopadhyay, J. Pannetier, and H. G. Von Schnering, Neutron diffraction study of the structural phase transition in SnS and SnSe, J. Phys. Chem. Solids. **47**, 879 (1986).

[46] T. Nagayama, K. Terashima, T. Wakita, H. Fujiwara, T. Fukura, Y. Yano, K. Ono, H. Kumigashira, O. Ogiso, A. Yamashita, Y. Takano, H. Mon, H. Usui, M. Ochi, K. Kuroki, Y. Muraoka, and T. Yokoya, Direct observation of double valence-band extrema and anisotropic effective masses of the thermoelectric material SnSe, Jpn. J. Appl. Phys. **57**, 010301 (2018).

[47] C. W. Wang, Y. Y. Y. Xia, Z. Tian, J. Jiang, B. H. Li, S. T. Cui, H. F. Yang, A. J. Liang, X. Y. Zhan, G. H. Hongg, S. Liu, C. Chen, M. X. Wang, L. X. Yang, Z. Liu, Q. X. Mi, G. Li, J. M. Xue, Z. K. Liu, and Y. L. Chen, Photoemission study of the electronic structure of valence band convergent SnSe, Phys. Rev. B **96**, 165118 (2017).